

1 Simultaneous reconstruction of scintillation light and
 2 ionization charge produced by 511 keV photons in
 3 liquid xenon : potential application to PET

4 P. Amaudruz^a, D. Bryman^{*,b}, L. Kurchaninov^a, P. Lu^b, C. Marshall^a,
 5 J. P. Martin^c, A. Muennich^a, F. Retiere^a, A. Sher^a

6 ^a*TRIUMF, 4004 Wesbrook Mall, Vancouver, BC, V6T 2A3*

7 ^b*Department of Physics and Astronomy, University of British Columbia, 6224
 8 Agricultural Road, Vancouver, BC, Canada V6T 1Z1*

9 ^c*University of Montreal, CP 6128 Succursale Centre-Ville, Montreal, Quebec, H3C 3J7
 10 Canada*

11 **Abstract**

12 In order to assess the performance of liquid xenon detectors for use in
 13 positron emission tomography we studied the scintillation light and ioniza-
 14 tion charge produced by 511 keV photons in a small prototype detector.
 15 Scintillation light was detected with large area avalanche photodiodes while
 16 ionization electrons were collected on an anode instrumented with low noise
 17 electronics after drifting up to 3 cm. Operational conditions were studied
 18 as a function of the electric field. Energy resolutions of $< 10\%$ (FWHM)
 19 were achieved by combining the scintillation light and ionization charge sig-
 20 nals. The relationship between scintillation light and ionization signals was
 21 investigated. An analysis of the sources of fluctuations was performed in
 22 order to optimize future detector designs.

23 *Key words:* Liquid Xenon, PET, Medical Imaging, TPC

24 *PACS:* 29.40.Gx, 87.57.-s, 87.57.uk

*corresponding author, Phone 001-604-222-7338, Fax 001-604-222-1074

Email addresses: amaudruz@triumf.ca (P. Amaudruz), bryman@phas.ubc.ca
 (D. Bryman), kurchan@triumf.ca (L. Kurchaninov), philipfl@phas.ubc.ca (P. Lu),
cammarsh@triumf.ca (C. Marshall), jpmartin@lps.umontreal.ca (J. P. Martin),
muennich@triumf.ca (A. Muennich), fretiere@triumf.ca (F. Retiere),
sher@triumf.ca (A. Sher)

25 1. Introduction

26 Positron Emission Tomography (PET) is a functional imaging technique
27 of growing importance in medical diagnostics. Its powers lie in the ability
28 to reveal biologically significant processes that can be used, for example, in
29 cancer screening and in studying neurodegenerative diseases. Conventional
30 PET detectors employ scintillating inorganic crystals [1] as the gamma ray
31 detection media. While crystal-based PET systems perform adequately for
32 many applications there is motivation for seeking improvements of resolu-
33 tions in energy, position, and time response to improve image quality and
34 increasing overall sensitivity. Liquid xenon (LXe) is another gamma ray de-
35 tector technology [2] applicable to high resolution PET which may result in
36 improved performance and reduced noise in images due to superior energy
37 resolution, true 3-dimensional position reconstruction, and the capability for
38 determining the Compton scattering sequence [3, 4, 5]. Energy resolution
39 of 7% (FWHM) has been reported in small LXe detector tests by combin-
40 ing scintillation light and ionization charge measurements [6]. Measuring
41 charge in a drift chamber has been shown to provide 3-D sub-millimeter spa-
42 tial resolution [7, 8] because electron diffusion is very small [9]. In addition,
43 sub-ns timing resolution has been achieved by measuring the scintillation
44 light [10]. Liquid xenon is also inexpensive compared to crystal detectors
45 commonly used for PET. Liquid xenon PET systems have the potential to
46 reduce detector contributions to PET to the level of intrinsic limitations
47 due to positron range and non-colinearity of the emitted photons.

48 This paper deals with the energy resolution obtained from light and
49 charge signals observed in a small LXe prototype detector as well as an
50 investigation of the components influencing it and the sources of uncertainty
51 which may inform the design of future detectors for PET.

52 2. Micro-PET Detector Design

53 We have developed a concept for a micro-PET detector shown in Fig. 1
54 that takes advantage of all the high resolution capabilities of LXe gamma ray
55 detectors. Scintillation light is measured by arrays of large area avalanche
56 photodiodes (LAAPD), which have been found to work well in LXe [11].
57 Charge measurement is achieved by using a time projection chamber (TPC),
58 an approach successfully demonstrated in [7]. Photons entering the LXe pro-
59 duce prompt scintillation light and ionization which drifts under an electric
60 field applied between the cathode and the anode of the TPC. The anode

61 module (not shown in Fig. 1) consists of a shielding grid followed by an
62 array of wires preceding the anode which is segmented into strips perpen-
63 dicular to the wires. The electron signal induced on the wires and collected
64 by the strips provides a two dimensional (x-y) position measurement of
65 the charge. The third coordinate (z) is obtained by measuring the elec-
66 tron drift time i.e. the difference between the time of the light flash and
67 the electron arrival time on the anode. Since every interaction is precisely
68 recorded, Compton scattering can be reconstructed giving information on
69 the direction of each incoming photon providing the possibility to suppress
70 accidental coincidences and scattering prior to reaching the detector.

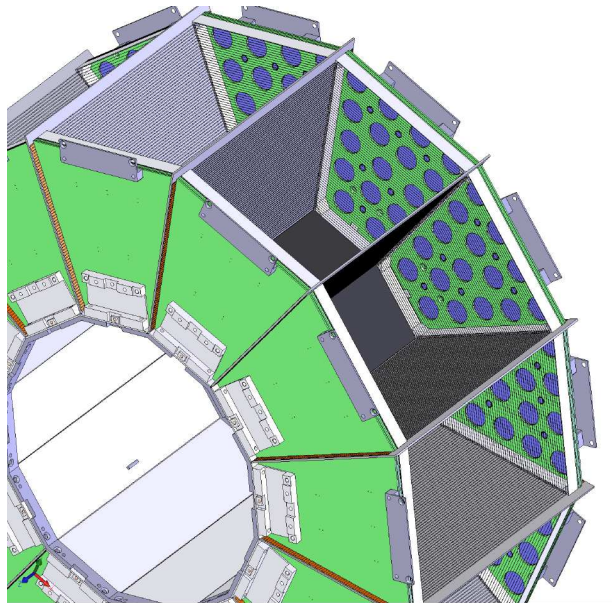


Figure 1: The LXe PET ring concept. Scintillation light and charge are measured in each of the 12 modules consisting of a LXe time projection chamber viewed by avalanche photodiodes.

71 The expectations for performance under operating conditions for PET
72 include sub-millimeter 3-D position resolution from charge, timing resolu-
73 tion of < 1 ns from scintillation light, energy resolution $< 10\%$ (FWHM)
74 combining light and charge signals, and the ability to reconstruct Compton
75 scattering. Spatial location of events obtained from the prompt distributed
76 light signals will be used to reduce the ambiguities of associating the scintil-
77 lation light and charge at high levels of activity. A simulation of the imaging

78 performance of this system will be presented in a future publication [12].

79 3. Small Chamber Prototype

80 3.1. Test Setup

81 As an initial step in studying LXe detectors for PET, we constructed
 82 a small test chamber (27 cm^3) for simultaneous measurements of light and
 83 charge. The test chamber is shown schematically in Fig. 2.

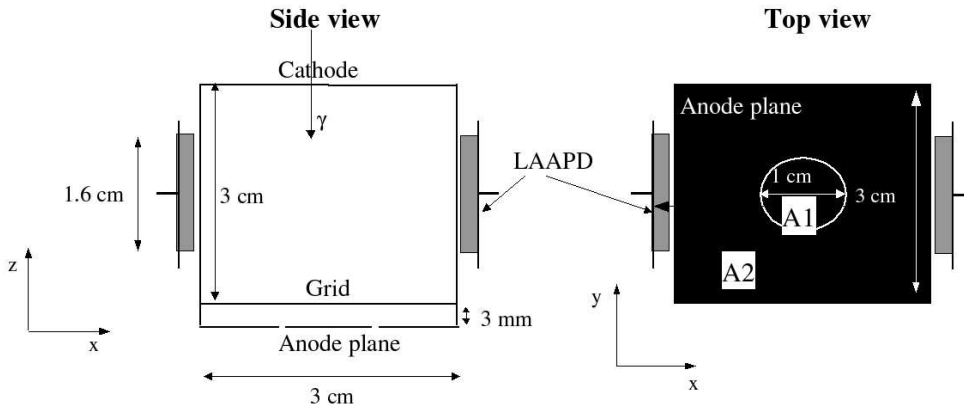


Figure 2: Schematic views of the small test chamber. The side view illustrates the drift direction between the cathode and anode, viewed by two LAAPDs immersed in the LXe. The top view shows the segmentation of the anode.

84 Scintillation light was detected by two 1.6 cm diameter windowless
 85 LAAPDs (Advanced Photonics Inc. [16]). The LAAPDs were located at
 86 the center of the drift region as shown in Fig. 2, 1.5 cm above the grid
 87 wires and 1.5 cm below the cathode. Charge was collected on a central 1 cm di-
 88 ameter electrode (A1) or on an outer electrode (A2). An electric drift field
 89 was applied between the cathode and a shielding grid separated by 3 cm.
 90 The electric field was formed by a field cage consisting of 9 wires with a
 91 spacing of 3 mm strung along the four walls of the chamber. The voltage
 92 was distributed by $100 \text{ M}\Omega$ resistors. The APDs were outside the field cage
 93 and the distance between the field cage wires and the APDs was 2 mm. The
 94 shielding grid consisted of 0.1 mm dia. wires spaced by 3 mm located 3 mm
 95 from the anode charge collection plane. The electric field between the grid
 96 wires and the anode was set higher than the drift field ensuring that all

97 the electrons pass through the grid [13]. In order to study the influence of
98 the drift field on quantities like charge and light production and the energy
99 resolution several settings were used. With the grid at ground potential
100 measurements were made with the negative cathode voltage set to 1, 3, 6,
101 and 8 kV, with the respective anode voltages set to 300, 600, 1200 and
102 1200 V. Photons of 511 keV emitted after annihilation of positrons from a
103 ^{22}Na source with an activity of $9.61 \cdot 10^5$ Bq and situated in a collimator with
104 an opening angle of 2° positioned 30 cm away from the cathode entered the
105 test chamber (along the z axis) through the cathode plane. The trigger was
106 generated by selecting signals in coincidence of both APDs and an external
107 NaI detector placed at a distance of 50 cm from the source observing the
108 full energy of the other 511 keV photon from the positron annihilation. The
109 probability to detect more than one event in the chamber at the same time
110 was less than 3%. The detector was operated at 15 psia and at temperatures
111 between 168 and 169 K. Before inserting the liquid in the vessel holding the
112 detector a bake-out in vacuum at $7.6 \cdot 10^{-6}$ T was performed for 6 days at
113 60°C to clean the components. The purification of the xenon was done in
114 the gas phase using two stages both with equipment from From NuPure
115 Corporation [14]: first, the heated getter (NuPure Omni 600) was used to
116 remove H_2O , O_2 , CO , H_2 , and N_2 to sub-ppb levels followed by a room
117 temperature getter (Eliminator 600 cg) to remove H_2O , O_2 , CO , H_2 , and
118 hydrocarbons to < 0.5 ppb. The lifetime of drifting ionization electrons
119 was used to indicate successful operation of the purification as discussed
120 below.

121 *3.2. Readout Electronics*

122 The two anodes segments and the grid wires (ganged together) were
123 connected to charge-sensitive amplifiers followed by a $1 \mu\text{s}$ time constant
124 RC-CR shaper. The amplifier was calibrated using a narrow pulse input
125 charge with a precision of 5%. The amplifier outputs were fanned out into
126 three branches:

- 127 1. A constant fraction discriminator followed by a time-to-digital con-
128 verter (TDC) CAEN model V1190B;
- 129 2. A charge sensitive analog-to-digital converter: 12 bit QDC CAEN
130 model V792 with gate adjusted to the drift time and pulse shape; and
- 131 3. A 20 MHz sampling waveform digitizer VF48 [15].

132 To get absolute charge values, the digitized waveform measured with the
133 VF48 was used for the analysis presented in sections 4 and 5. Because the

134 QDC had a better signal to noise ratio it was used to determine the energy
135 resolution in section 6 which did not require absolute charge calibration.
136 The other reason the QDC was not used for absolute values was due to the
137 very short pulse used for calibration. The longer chamber signal would not
138 have been fully integrated within the window set.

139 The observed range of noise of the amplifier was 700-1100 electrons due
140 to varying external sources of induced noise. To reach the optimal position
141 resolution, a signal to noise ratio larger than 5 was desirable requiring the
142 electronics noise to be kept below 1000 electrons equivalent noise charge
143 (ENC). A typical signal was expected to be at least 10 000 e-, as long as
144 the electron attachment during the drift was small.

145 The LAAPD voltages were set so that their gains were 500 and each was
146 connected to a current-sensitive preamplifier with a pulse width of 50 ns and
147 10^4 electrons ENC. The amplifier signal was split into 3 branches:

- 148 1. Discriminator and TDC;
- 149 2. QDC CAEN model V792 with a gate of 100 ns; and
- 150 3. 1 GHz waveform digitizer CAEN model V1729.

151 Solid angle calculations showed that 12% of the scintillation photons
152 reached the LAAPDs when the gamma interaction took place in the center
153 of the chamber.

154 **4. Charge Collection**

155 The grid wires shielded the anodes from the current induced by the
156 drifting electrons. Once the ionization electrons passed the grid wires the
157 signal on the anode started to build up with a pulse shape that was largely
158 independent of the z position of the primary interaction although electro-
159 static calculations showed that the current pulse shape depended on the x-y
160 distance of the electron cloud from the individual grid wires. Furthermore,
161 depending on the drift velocity (typically 0.15 to 0.21 cm/ μ s), the current
162 induced on the anodes lasted 1.5 to 2 μ s.

163 The waveforms measured on the grid and on the two anodes provided
164 information about the location of charge creation and Compton scattering if
165 multiple charge pulses were observed. The time of charge arrival relative to
166 the light signal gave information about the position along the drift direction
167 of the electrons.

168 Figure 3 shows examples of four charge waveform events recorded by
169 the 20 MHz waveform digitizers chosen to illustrate several types of events.

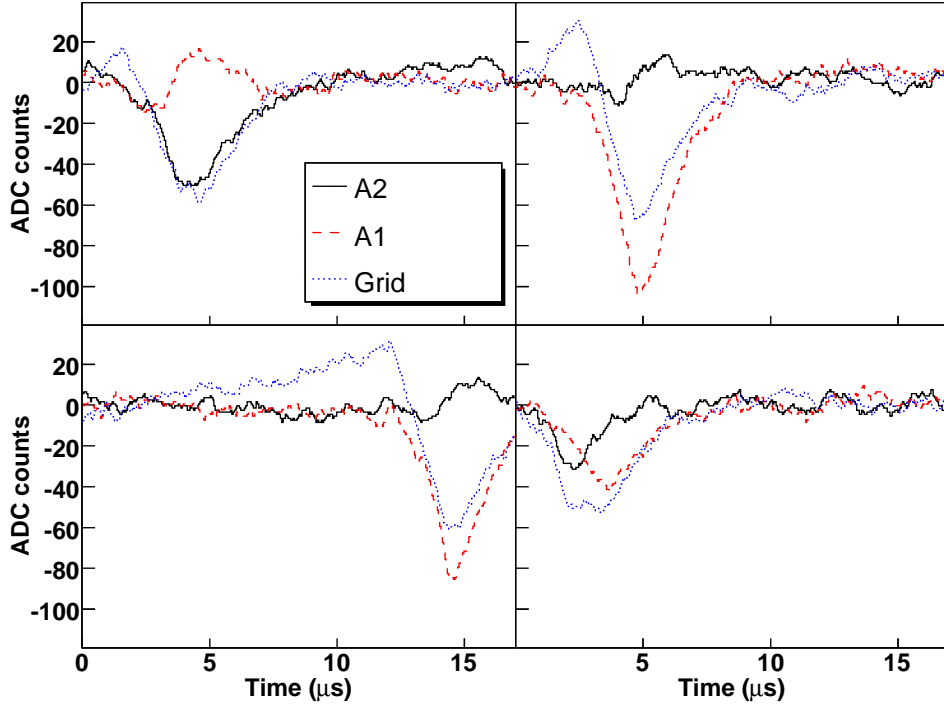


Figure 3: Example of waveforms with a 2 kV/cm drift field. Central anode A1 (dashed line), peripheral anode A2 (solid line), grid (dotted line).

170 In the upper two plots the charge was created roughly at the same z posi-
 171 tion; in the left plot the signal of the central anode (A1) integrated to zero
 172 and the anode A2 collected the charge, whereas in the right hand plot the
 173 interaction deposited the full charge on the central anode A1. The lower
 174 left panel shows an event originating close to the cathode plane, resulting
 175 in a measured drift time of 15 μs . The charge was collected by the central
 176 anode. The bipolar shape of the grid signal is clearly visible. The waveform
 177 measured on the grid depends on the z position of the interaction and is
 178 also influenced by electrons collected by the grid. The lower right panel
 179 shows two photon interactions, presumably one Compton scattering and
 180 one photo-electric interaction. One interaction took place above A1 and
 181 one above A2. The interactions were also separated in the drift direction so
 182 that a two peak structure is visible in the grid waveform. Simulations of the
 183 setup showed that only a small fraction (less than 5%) of events fully con-

184 tained on A1 have multiple hits that can be detected. The total charge for
185 these events however is not significantly different from the events with just
186 one interaction. For this analysis we did not treat them separately since we
187 were primarily interested in the total charge deposited on the anode. Better
188 separation of multiple photon interactions on an event by event basis will
189 be possible with finer segmentation of the readout electrodes and shorter
190 shaping time.

191 The purity of the LXe has an impact on charge collection. In the current
192 setup we achieved an electron lifetime of 200 μs using purification in the gas
193 phase with heated getters¹. We estimated that the level of purity obtained
194 would result in a loss of 8% of the electrons due to attachment.

195 For the analysis in this paper we selected events where no net charge
196 was measured on A2. By demanding the absence of charge on A2 the region
197 of A1 in which events were accepted was smaller than its physical size since
198 charge depositions close to the edge of A1 induced charge on A2. The
199 effective radius of the tube in which events were accepted was estimated to
200 be 0.45 cm compared to the A1 radius of 0.5 cm.

201 Figure 4 shows the distribution of charge due to 511 keV photons in-
202 cident on the chamber as measured on A1 as a function of the drift time
203 for a 1 kV/cm drift field. The shape of the distribution is the same for all
204 drift fields. The 511 keV band rises sharply in less than 1 μs , and then falls
205 slowly until the cutoff which corresponds to the edge of the chamber. The
206 sharp rise corresponds to photons interacting between the grid and anode.
207 In that case the electronics, which is not sensitive to the charge induced
208 by the much slower drifting ions, measures only a fraction of the charge
209 which is approximately proportional to the distance between the anode and
210 the interaction point. When the interaction point is between the grid and
211 the cathode, the measured charge should be independent of the interaction
212 position. The decline of measured charge with increasing drift times is due
213 to electron attachment by impurities in the LXe.

214 Compton scattering interactions are evident below the 511 keV band.
215 They are due to photons entering the chamber with less than 511 keV
216 because they have scattered in the passive detector material, mostly the 2
217 cm of LXe between the vessel wall and the cathode, and to photons escaping
218 after a Compton scattering interaction in the liquid.

¹A problem occurred with the purification system during the data taking with the NaI coincidence trigger used in this paper resulting in an electron lifetime of 90 μs for much of the data presented here.

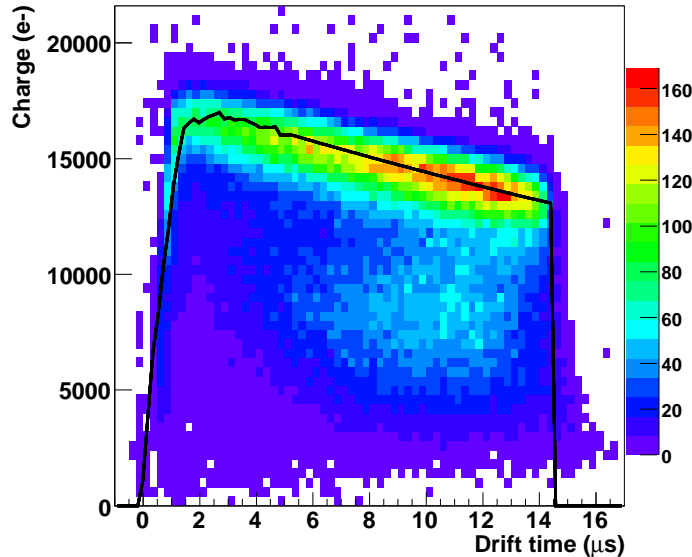


Figure 4: Charge collection as a function of drift time for a 1 kV/cm drift field. The curve is a fit based on parametrization obtained from current calculations for energy deposits of 511 keV. The scale on the right corresponds to the number of events that occurred at a specific time with a certain charge deposition.

219 We performed a fit of the 511 keV band to extract the drift velocity v_d ,
 220 the total charge Q_{tot} produced in the photon interaction and the attenua-
 221 tion length. The values obtained for these quantities are listed in Table 1
 222 with their statistical uncertainties from the fits. The charge yield Q_{tot}/Q_0
 223 is also shown along with Q_{tot} which is the measured charge corrected for
 224 attachment and electronics calibration and Q_0 is the ratio of the energy
 225 deposited by the γ -ray and the average energy to produce an electron ion
 226 pair: $Q_0 = E_\gamma/W$ with $W=15.6$ eV [17].

227 Figure 5 shows the comparison of our results for the charge yield to
 228 the values obtained in [6] and [18]. Our results lie in between the two
 229 previous measurements of the charge yield. The obtained drift velocity was
 230 in agreement with previous measurements in [19].

E_d [kV/cm]	v_d [cm/ μ s]	Q_{tot} (511 keV e^-)	τ [μ s]	$\frac{Q_{tot}}{Q_0}$
0.33	0.16 ± 0.01	$19\,707 \pm 55$	94 ± 3	0.60
1	0.18 ± 0.01	$23\,372 \pm 59$	61 ± 2	0.71
2	0.20 ± 0.01	$25\,092 \pm 100$	76 ± 5	0.77
2.66	0.20 ± 0.01	$24\,761 \pm 35$	60 ± 1	0.76

Table 1: Drift velocity (v_d), number of electrons (Q_{tot}), electron lifetime τ and charge yield observed for different electric fields (E_d).

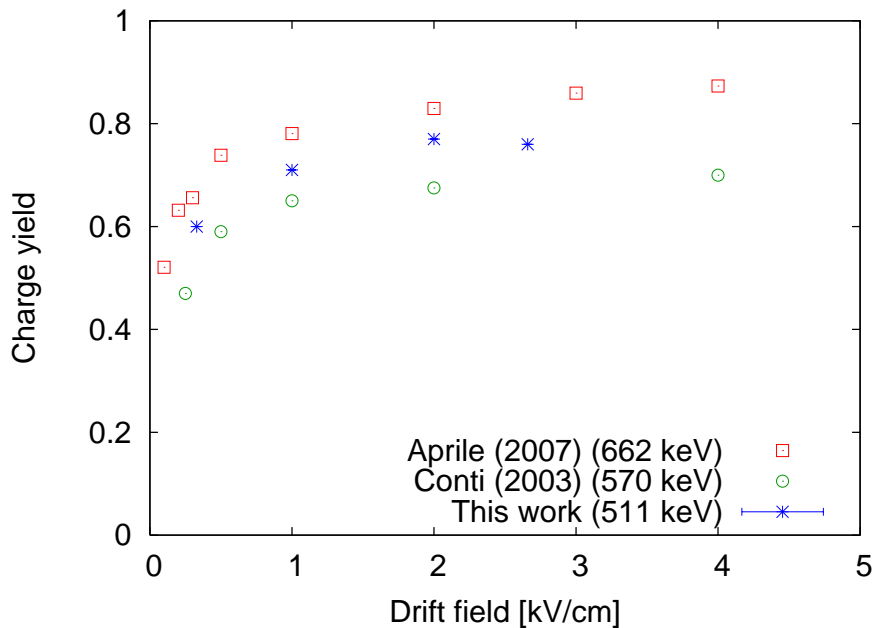


Figure 5: Charge yield measured by different groups at different γ -ray energies: this work marked with \star , [6] with \square and [18] with \circ .

231 5. Light Collection

232 Scintillation light was detected by the LAAPDs located on two sides of
 233 the chamber. Figure 6 shows the sum of the number of photons measured
 234 by both LAAPDs as a function of the electron drift time for the events
 235 where all the charge was collected on the central anode.

236 The bell shape in Fig. 6 is due to variations of the solid angle with
 237 drift distance which can be calculated by integrating over the LAAPD area
 238 for a given location in the chamber assuming no reflections occurred in

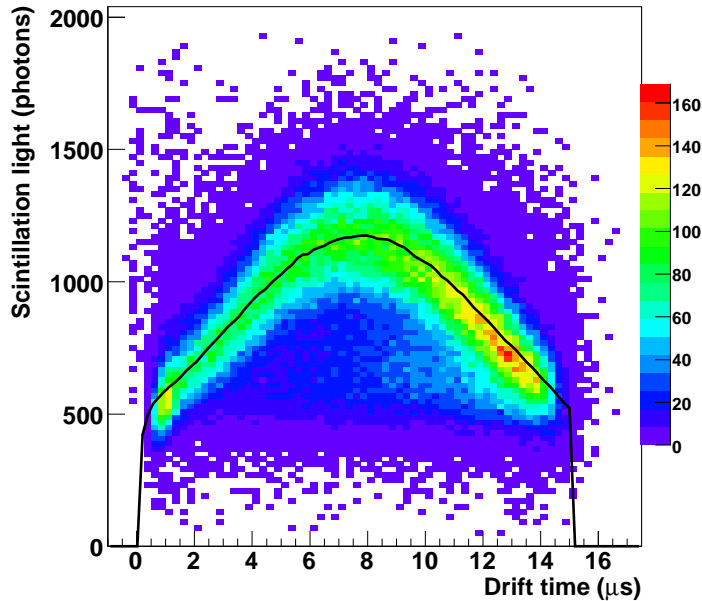


Figure 6: Light collection as a function of drift time for a 1 kV/cm drift field at 511 keV. The curve is a fit based on parametrization obtained from solid angle calculations. The scale on the right corresponds to the number of events that occurred at a specific time with a certain charge deposition.

239 the chamber walls. The solid angle varied significantly with the position
 240 of the photon interaction. The arrival time of the electrons provided a
 241 handle on the solid angle variation in the drift direction. However, there
 242 was no information about the position of the interaction within the disk
 243 defined by A1. When the LAAPDs were used independently, the solid
 244 angle variation within this disk introduced a 22% fluctuation in the light
 245 collection. Combining both LAAPDs reduced the fluctuation to 6%.

246 We fitted the distribution in fig. 6 using a parametrization of the solid
 247 angle, with the total number of photons and the drift velocity as free pa-
 248 rameters. The fit parameters are shown in Table 2. The drift velocity is
 249 consistent with the one extracted from the fit to the charge distribution.
 250 The total number of photons drops with increasing drift voltage in agree-
 251 ment with previous measurements [6, 18]. The number of photons actually
 252 created within the detector was not extracted in this analysis because we
 253 did not measure the photon detection efficiency (PDE) of the LAAPDs.
 254 One of the LAAPDs detected more photons than the other one, which sug-

255 gests that there may be a variation of the PDE between LAAPDs². In
 256 the results given in Table 2, we have assumed 100% PDE for the LAAPD
 257 that exhibited a more stable operation and scaled the light measured by the
 258 other LAAPD accordingly introducing a systematic uncertainty because of
 259 the unknown efficiency (which may be up to 50%). Uncertainties also orig-
 260 inated from the fact that the ratio between the mean value measured by
 261 the two LAAPDs varied between data sets by 10%. The light yield was
 262 computed using a value of 13.8 eV [17] needed to create one photon at zero
 263 drift field resulting in $S_0 = 37029$ photons. N_{tot} is the number of measured
 264 photons corrected for the solid angle of the geometry but not corrected for
 265 the photo detection efficiency of the LAAPDs.

E_d [kV/cm]	v_d [cm/ μ s]	N_{tot} (511 keV e^-)	N_{tot}/S_0
0.33	0.15 ± 0.01	$12\ 161 \pm 1269$	0.33
1	0.18 ± 0.01	$10\ 113 \pm 1055$	0.27
2	0.20 ± 0.01	9243 ± 964	0.25
2.66	0.21 ± 0.01	7936 ± 828	0.21

Table 2: Electric field (E_d), drift velocity (v_d), number of photons (N_{tot}) and light yield observed (see text) for 511 keV photon interactions.

266 Figure 7 shows the comparison of our results with values obtained in
 267 [6] and [18]. If the quantum efficiency of the LAAPDs was 60%, which
 268 later results presented here suggest, our results would be in agreement with
 269 previous measurements.

270 6. Light and Charge Combination

271 To study the energy resolution we focused on the central region of the
 272 chamber by selecting events with no charge on A2 and choosing a time
 273 window in the drift direction corresponding to 2 mm drift located on the
 274 axis of the LAAPDs where the light collection is maximal as shown in Fig. 6.
 275 The charge signals were corrected for attenuation and the light signals for
 276 the difference between the two LAAPDs and the solid angle dependence in
 277 the drift direction. Resolution results are given as the standard deviation
 278 (σ) of a Gaussian distribution unless otherwise stated. Figure 8 shows

²This may explain the apparent discrepancy between measurements made by different groups [21]

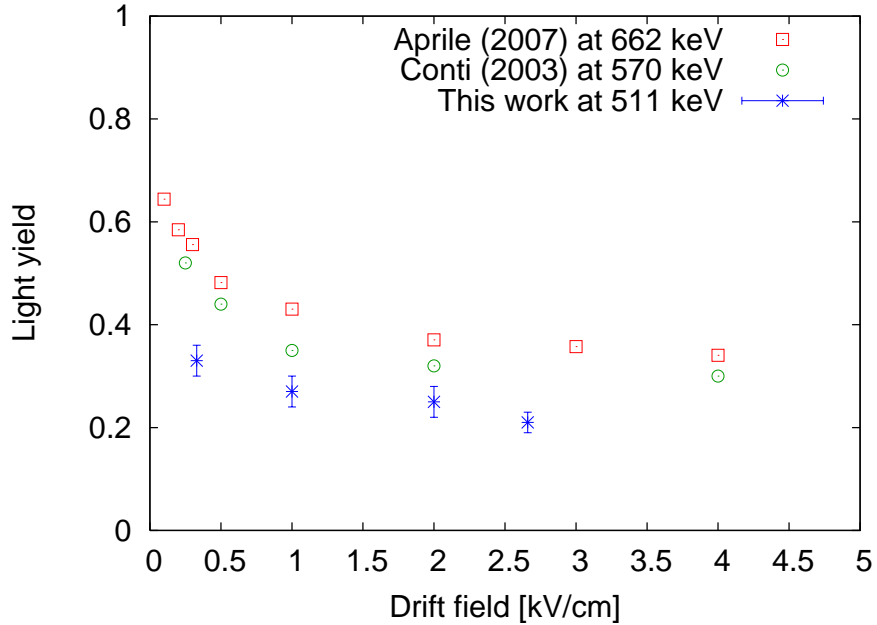


Figure 7: Light yield relative to the maximum yield measured by different groups at different γ -ray energies: this work marked with \star , [6] with \square and [18] with \circ .

279 the analysis of a data run at a drift field of 2.66 kV/cm. Evaluating the
 280 charge and light signals separately gave energy resolutions of 12.1% for
 281 light and 5.4% for charge by fitting the spectra (shown in the upper plots of
 282 Fig. 8) with a sum of two Gaussians and evaluating the mean and width of
 283 the 511 keV peak. The energy resolution can be improved significantly by
 284 combining the information from light and charge using the anti-correlation
 285 of the two signals [6, 18, 20]. The lower left plot of Fig. 8 shows the linear
 286 anti-correlation between the light and charge measurement and the axis
 287 of the ellipse. Selecting the 511 keV region of the photo-electric-peak the
 288 correlation angle was obtained from a linear fit which provided the axis
 289 of the charge-light ellipse. Projecting the data points along this axis as
 290 described in [6] gave the overall energy resolution. The correlation angle
 291 given here depended on the detector geometry and the efficiency to measure
 292 light and charge separately. The upper left plot shows the charge spectrum
 293 collected on the anode which is equal to a projection of the correlation along
 294 the light axis. In the upper right plot the projection of the correlation
 295 along the charge axis can be seen, giving the spectrum of the collected

296 light. The lower right plot demonstrates the improved energy resolution
 297 of the combined spectrum when projecting along the correlation axis and
 298 normalizing to the mean charge. The sum of three Gaussians was used as
 299 the fit function to account for the three contributions to the spectrum: the
 300 Compton region (C), the photoelectric peak (P), and scattered events (S)
 301 which lost energy outside the detector, mostly in the LXe before entering
 302 the chamber.

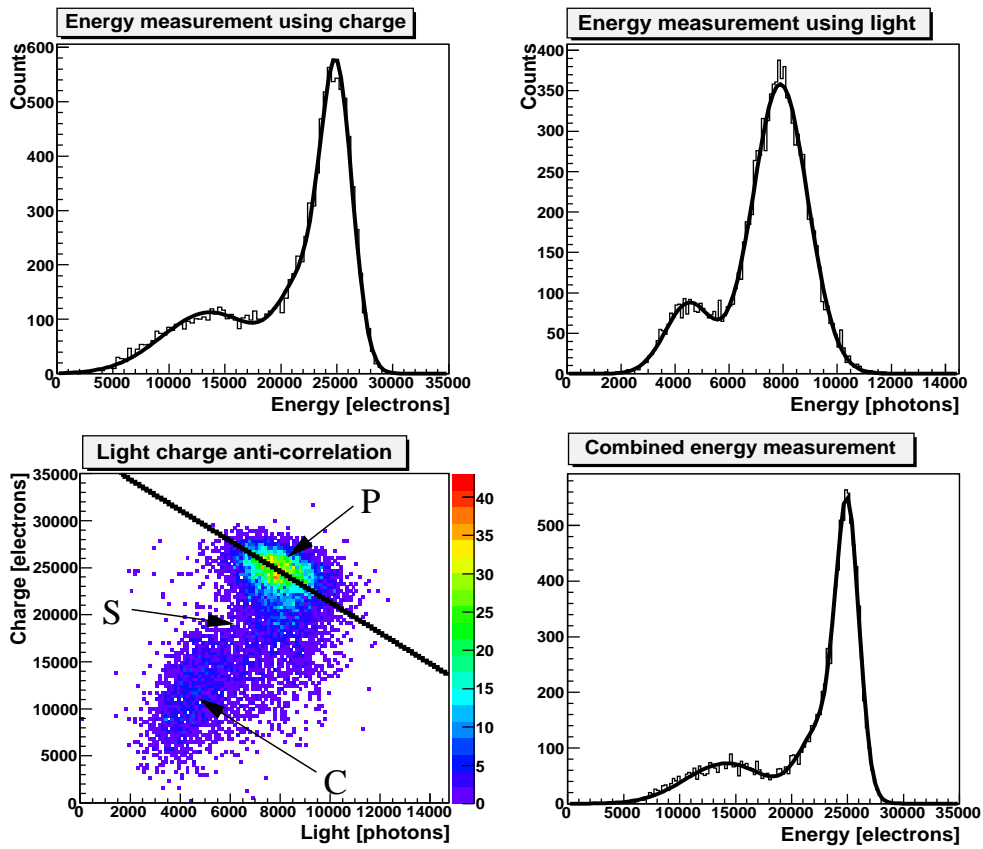


Figure 8: The observed charge spectrum (upper left plot), light spectrum (upper right plot), correlation between light and charge signals (lower left plot), and combined spectrum using the correlation (lower right plot) for 511 keV photons with a drift field of 2.66 kV/cm. The data points in the correlation plot (lower left) that are not part of the Compton (C) or the photoelectric peak (P) are due to photons that scattered outside the detector (S). The linear fit (solid line) giving the axis of the correlation ellipse is depicted as well. The fits shown (solid lines) were made with a sum of 3 Gaussians (upper left and lower right plot) or 2 Gaussians (upper right plot).

303 Another variable to quantify the anti-correlation between light and charge
 304 is the correlation coefficient ρ [22]. Assuming that the probability for a re-
 305 combining electron-ion pair to produce a scintillation photon is 1 and the
 306 detector would be able to measure light and charge with 100% efficiency
 307 and perfect resolution, ρ should be -1. Deviation from -1 could be due to
 308 other sources of fluctuations like density fluctuations or delta electrons as
 309 discussed in [23] and the references within.

310 Table 3 gives the results of the analysis for different drift fields. The
 311 best combined energy resolution reached for these data sets was 4.1% at
 312 2.66 kV/cm drift field (see below).

E_d [kV/cm]	Energy resolution [%]			θ_{corr} [°]	ρ
	light	charge	combined		
0.33	13.5 ± 0.2	7.3 ± 0.5	4.7 ± 0.1	56	-0.46
1	12.2 ± 0.2	6.0 ± 0.3	4.3 ± 0.3	59	-0.34
2	12.8 ± 0.5	7.0 ± 0.6	4.8 ± 0.4	62	-0.34
2.66	12.1 ± 0.1	5.4 ± 0.2	4.1 ± 0.1	58	-0.26

Table 3: Energy resolutions (σ) observed at different drift fields for light and charge separately and combined result using the correlation.

313 7. Discussion of Error Sources

314 In this section we discuss contributions to the energy resolution that
 315 were due to detector inefficiencies or physics constraints like light-charge-
 316 fluctuations. When a photon interacts there is an initially produced number
 317 of ionization charges and scintillation photons which is modified by recom-
 318 bination dependent on the presence of an applied electric field. Table 4
 319 summarizes the variables used in the calculation of error contributions.

	Charge	Scintillation light
Initial	Q_i	S_i
Final	$Q_f = Q_i[1 - F_r(E_d)]$	$S_f = S_i + Q_i F_r(E_d) P_{e \rightarrow h\nu}$
Measured	$Q_m = A Q_f$	$S_m = F_{\Omega} \epsilon S_f$

Table 4: Parameters used in the discussion of energy resolution as described in the text.

320 Q_i, Q_f and Q_m (S_i, S_f and S_m) are the numbers of initially produced,
 321 post-recombination, and measured charge (light) signals respectively. $F_r(E_d)$

322 is the fraction of electron-ion pairs that recombine for a given electric field
 323 E_d , and $P_{e \rightarrow h\nu} = 1$ [6] gives the probability for a recombining electron-ion
 324 pair to produce a scintillation photon. Impurities may capture some elec-
 325 trons, which is accounted for by an attenuation parameter A , which depends
 326 on the electron drift distance. The photo-detectors have a photo-detection
 327 efficiency ϵ and cover a fraction of the total solid angle F_Ω .

328 7.1. Charge

329 The charge resolution is dominated by electronics noise and charge-light
 330 fluctuation. The charge-light fluctuation is expressed by the fluctuation of
 331 the recombination fraction F_r , ΔF_r . The charge resolution can then be
 332 written as

$$\left(\frac{\Delta Q_m}{Q_m}\right)^2 = \left(\frac{ENC_q}{Q_m}\right)^2 + \left(\frac{\Delta F_r}{1 - F_r}\right)^2 + \frac{1 - A}{Q_m} \quad (1)$$

333 where the first term on the right describes the electronics noise of the am-
 334 plifier, the second term quantifies the light-charge fluctuation, and the third
 335 contribution is the attachment factor which is negligible. ΔF_r describes the
 336 fluctuation of the recombination and will also occur in the discussion of the
 337 error sources for the light measurement in the next section. Table 5 gives
 338 values for the error contributions to the energy resolution obtained from the
 339 charge measurement. Also shown is the intrinsic energy resolution found by
 340 subtracting the noise of the electronics from the measured resolution. The
 341 only unknown variable contributing to the error of the energy resolution is
 342 ΔF_r which can be calculated once the intrinsic energy resolution is known.
 343 The values for ΔF_r obtained can also be found in Table 5.

E_d [kV/cm]	Measured res. [%]	Noise [%]	Intrinsic res. [%]	ΔF_r [%]
0.33	7.31 ± 0.54	5.03 ± 0.04	5.3 ± 1.5	3.2 ± 0.9
1	6.04 ± 0.33	4.22 ± 0.03	4.3 ± 0.9	3.1 ± 0.7
2	7.00 ± 0.62	4.29 ± 0.03	5.5 ± 1.6	4.2 ± 1.2
2.66	5.43 ± 0.17	3.48 ± 0.03	4.2 ± 0.4	3.2 ± 0.3

Table 5: Contribution of error sources to the energy resolution obtained from the charge measurement.

344 *7.2. Light*

345 The fluctuations in the LAAPD specified as the excess noise factor
 346 $F(M) = 2 + kM$ is dependent on the gain M and affects the resolution.
 347 For this setup with $k = 0.001$, $F(M) = 2.5$. Furthermore, the LAAPD gain
 348 $< 10^3$ requires that low noise electronics must be used to further amplify
 349 the signal, which adds electronic noise ENC_s . Another source of fluctua-
 350 tions arises because the solid angle seen by the photo-sensor may vary on
 351 an event-by-event basis since the solid angle changes with the position of
 352 the photon interaction within A1. This fluctuation can be corrected for if
 353 the interaction position is known well from the ionization signal.

354 Neglecting other detection fluctuations, the light signal resolution for
 355 our setup can be written as:

$$\begin{aligned}
 \left(\frac{\Delta S_m}{S_m}\right)^2 &= \left(\frac{ENC_s}{MS_m}\right)^2 + \frac{F(M)}{S_m} \\
 &+ \left(\frac{\Delta F_\Omega}{F_\Omega}\right)^2 + \left(\frac{P_{e \rightarrow h\nu} Q_i \Delta F_r}{S_f}\right)^2 \\
 &+ \frac{F_r Q_i P_{e \rightarrow h\nu} (1 - P_{e \rightarrow h\nu})}{S_f^2}
 \end{aligned} \tag{2}$$

356 where the first term on the right represents the electronics noise, the
 357 second term gives the contribution from fluctuations in the LAAPD gain,
 358 the third term is the fluctuation of the solid angle due to the position of
 359 the light creation inside the chamber and the fourth term describes the
 360 light-charge fluctuation. The contribution of the fluctuation in $P_{e \rightarrow h\nu}$ given
 361 by the last term is negligible or exactly zero if $P_{e \rightarrow h\nu} = 1$. Table 6 gives
 362 values for the error contributions to the measured energy resolution from the
 363 scintillation light. The solid angle fluctuation amounted to 5.6% and was
 364 independent of the drift field. Also shown is the intrinsic energy resolution
 365 found when subtracting those error sources due to the detector from the
 366 measured resolution. ΔF_r was calculated again and can be compared to
 367 the values obtained from the charge measurement. The values for ΔF_r
 368 from both the light and charge measurements are in good agreement within
 369 statistical errors providing a consistency check for the error analysis.

370 *7.3. Combination*

371 Combining the light and charge allows improvement to the resolution
 372 by canceling the fluctuations of F_r by making use of the anti-correlation,

E_d [kV/cm]	Measured res. [%]	Noise [%]	LAAPD fluct. [%]	Intrinsic res. [%]	ΔF_r [%]
0.33	13.5 ± 0.2	3.3	0.46	9.6 ± 0.4	5.8 ± 1.3
1	12.2 ± 0.2	4.0	0.55	6.8 ± 0.8	3.3 ± 1.0
2	12.8 ± 0.5	5.1	0.56	7.1 ± 1.7	3.1 ± 1.2
2.6	12.1 ± 0.1	4.7	0.63	5.5 ± 0.5	2.5 ± 0.8

Table 6: Contribution of error sources to the energy resolution obtained using the light measurement.

373 provided the measured charge is corrected for attenuation and the measured
374 light for solid angle and PDE:

$$E_c = \frac{Q_m}{A} + \frac{S_m}{F_\Omega \epsilon} \quad (3a)$$

$$= Q_f + \frac{S_f}{P_{e \rightarrow h\nu}} \quad (3b)$$

$$= Q_i (1 - F_r) + \frac{S_i}{P_{e \rightarrow h\nu}} + Q_i F_r \quad (3c)$$

$$= Q_i + \frac{S_i}{P_{e \rightarrow h\nu}} \quad (3d)$$

375

376 where E_c is the energy measured by combining the charge and light
377 signals: In eq. 3a the light and charge signals were combined; eq. 3b and
378 eq. 3c made use of the formulas in Table 4; and in eq. 3d F_r was eliminated.
379 The remaining uncertainty in the combined energy resolution is then:

$$\begin{aligned} \Delta E_c^2 &= \frac{1}{\epsilon^2 F_\Omega^2} \left[\left(\frac{ENC_s}{M} \right)^2 + F(M) S_m + \left(\frac{\Delta F_\Omega S_m}{F_\Omega} \right)^2 \right] \\ &+ \left(\frac{ENC_q}{A} \right)^2 \\ &+ \frac{Q_f (1 - A)}{A} + \frac{F_r Q_i (1 - P_{e \rightarrow h\nu})}{P_{e \rightarrow h\nu}} \end{aligned} \quad (4)$$

380 where the first term on the right hand side (in brackets) originated
381 from the light signal contribution and the second term from the charge
382 measurement. The last two terms describing the contributions from the
383 binomial statistics of A and $P_{e \rightarrow h\nu}$ are negligible.

384 Table 7 gives the calculated values for the combined energy resolution
 385 $\Delta E_c/E_c$. The intrinsic combined energy resolution given in the last column
 386 of table 7 was obtained by subtracting $\Delta E_c/E_c$ in quadrature from the mea-
 387 sured values. The solid angle was 12% and the efficiency ϵ for the LAAPDs
 388 was assumed to be 1.

E_d [kV/cm]	Meas. comb. res [%]	$\Delta E_c/E_c$ [%]	Intr. comb. res. [%]
0.33	4.74 ± 0.09	4.0 ± 0.1	2.5 ± 0.4
1	4.31 ± 0.26	3.7 ± 0.1	2.3 ± 1.0
2	4.78 ± 0.35	3.8 ± 0.1	2.9 ± 1.2
2.66	4.14 ± 0.10	3.3 ± 0.1	2.5 ± 0.4

Table 7: Contribution of error sources and corrected intrinsic energy resolution for combined charge-light measurement.

389 The intrinsic correlation coefficient was calculated but showed a large
 390 uncertainty due to the impact of the uncertainty on ΔF_r .

391 Another consistency check of the formulas presented here can be made
 392 by extracting the factor $\epsilon P_{e \rightarrow h\nu}$ in two different ways from the data. We
 393 cannot disentangle the efficiency from the probability but the product can
 394 be obtained from the correlation angle of the 511 keV cloud by writing
 395 Q_m/A as a function of S_m/F_Ω with the slope m describing the axis of the
 396 ellipse:

$$\frac{Q_m}{A} = Q_f = m \frac{S_m}{F_\Omega} + const. \quad (5)$$

$$\implies \theta_{corr} = \arctan \left(\frac{-1}{\epsilon P_{e \rightarrow h\nu}} \right)$$

397 The results are listed in Table 8. The mean value over all runs was
 398 $\epsilon P_{e \rightarrow h\nu} = 0.60 \pm 0.03$.

399 The other method for extracting $\epsilon P_{e \rightarrow h\nu}$ is to find the slope from the
 400 plot of the mean values of light vs. charge (coordinates of the center of the
 401 ellipse) for each electric field setting. This is shown in Fig. 9. The linear fit
 402 to this data gave a slope of $\epsilon P_{e \rightarrow h\nu} = 0.7 \pm 0.3$ which agrees with the value
 403 obtained from the event-by-event method. This result would be consistent
 404 with $P_{e \rightarrow h\nu} = 1$ if the efficiency of the APDs were 60%.

E_d [kV/cm]	θ_{corr}	$\epsilon P_{e \rightarrow h\nu}$
0.33	56.2	0.67 ± 0.03
1	58.7	0.61 ± 0.11
2	62.3	0.53 ± 0.30
2.66	58.5	0.61 ± 0.05

Table 8: Calculating $\epsilon P_{e \rightarrow h\nu}$ on event by event basis.

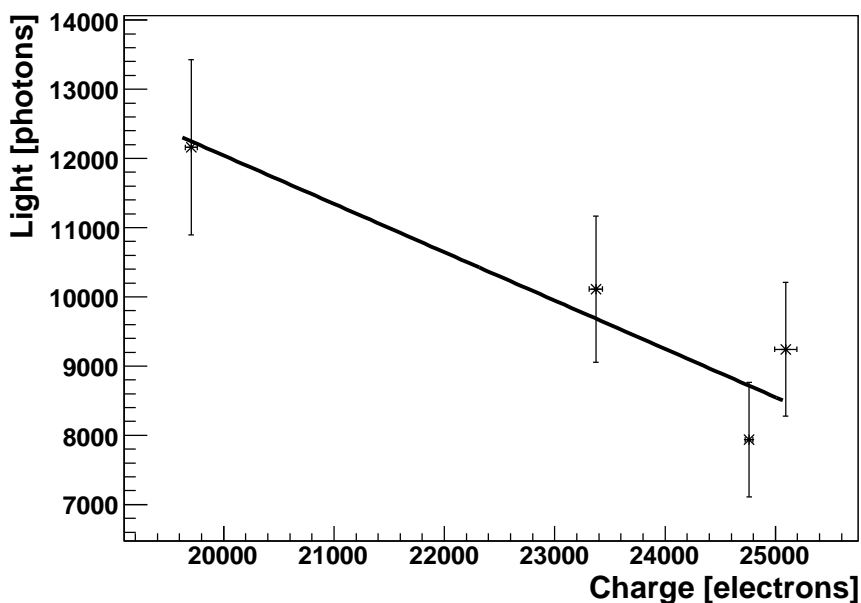


Figure 9: Method of extracting $\epsilon P_{e \rightarrow h\nu}$ from mean values of the correlation cloud parameters described in the text. The solid line is the linear fit to the data.

405 7.4. Improving Light Resolution using Position Reconstruction

406 In the current system, the energy resolution contribution from light was
407 partially limited by the uncertainty in the position of the light source due to
408 the 1 cm dia. size of A1 i.e. from the fluctuation of the solid angle within A1.
409 Applying the formulas presented above to a Geant4 [24] simulation, it was
410 found that knowing the position of the light signal to 1 mm would improve
411 the light resolution by about 1.5% and the combined resolution by up to
412 0.5% giving 10% for light alone and 3.6% for the combination of charge and
413 light, consistent with the resolution reported in [6]. Table 9 summarizes the

414 values obtained with the simulation comparing the two cases of not knowing
 415 the position of the interaction within A1 and being able to correct for it.

	Light res. [%]	Charge res. [%]	Combined res. [%]
Measured	12.1 ± 0.1	5.4 ± 0.2	4.1 ± 0.1
Simulated	12.0 ± 0.2	5.4 ± 0.1	3.9 ± 0.1
Corrected	10.4 ± 0.2	5.4 ± 0.1	3.6 ± 0.1

Table 9: Energy resolutions obtained from the simulation with (corrected) and without (simulated) the correction for the position of the interaction within A1 in comparison with the measured resolutions. The charge resolution was not affected by the correction.

416 8. Summary and Conclusion

417 Measurements have been made of the response of a liquid xenon drift
 418 chamber to irradiation by 511 keV photons. Using a model accounting
 419 for the sources of uncertainty in the energy resolution we also determined
 420 values for the intrinsic energy resolutions. Figure 10 summarizes the results
 421 for charge, light and combined energy resolution as a function of the drift
 422 field. The main error contribution to the combined energy resolution, apart
 423 from the solid angle fluctuations which can be eliminated by utilizing the
 424 position measurement, originated from the APD gain fluctuation and the
 425 anode noise. Both were about of 2.7%.

426 Figure 11 depicts the values for the intrinsic energy resolutions obtained
 427 by subtracting the detector contributions from the values in fig. 10. The
 428 error bars given are statistical.

429 Based on these results, the combined energy resolution of <3.5% (or
 430 < 8% FWHM) would be anticipated in a detector configuration suitable for
 431 applications to PET which would have comparable light collection efficiency
 432 to the prototype detector described above and <1 mm spatial resolution.
 433 Reducing the anode to grid spacing to 1 mm and the grid wire spacing to
 434 1 mm will reduce the width of the pulses and minimize the dependence of
 435 the pulse shape on the location of the electron cloud. Further improvements
 436 are foreseen in areas including purification and low noise electronics.

437 Acknowledgments

438 We thank R. Bula, M. Constable, and C. Lim for their technical con-
 439 tributions to this work and P. Gumplinger for assistance with simulations.

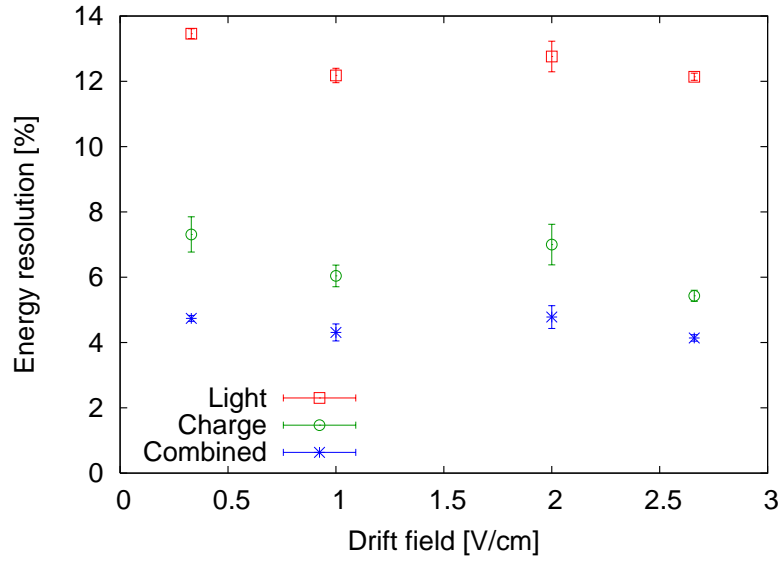


Figure 10: Energy resolution from charge (○) and light (□) measurements as well as the combined (★) resolution for different drift fields.

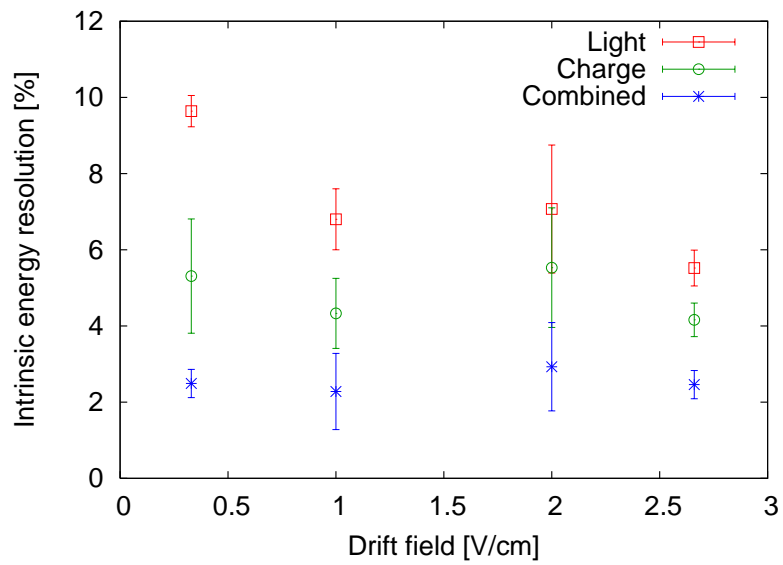


Figure 11: Intrinsic energy resolution from charge (○) and light (□) measurements as well as the combined (★) intrinsic resolution for different drift fields.

440 We also thank E. Aprile and E. Conti for providing information about their
441 work. This work was supported in part by the Canada Foundation for In-
442 novation, the University of British Columbia, and TRIUMF which receives
443 federal funding via a contribution agreement through the National Research
444 Council of Canada.

445 References

- 446 [1] See , for example, Jin Su Kim *et al.*, *Performance Measurement of the microPET*
447 *Focus 120 Scanner*, The Journal of Nuclear Medicine, Vol. **48** (2007), No. 9, p. 1527.
- 448 [2] E. Aprile *et al.*, *Noble Gas Detectors*, Wiley-VCH, Berlin, 2006, ISBN-10: 3-527-
449 40597-6.
- 450 [3] K. Giboni *et al.*, *Compton Positron Emission Tomography with a Liquid Xenon*
451 *Time Projection Chamber*, JINST **2** (2007) P10001.
- 452 [4] Chepel, V.Y., *A new liquid xenon scintillation detector for positron emission tomo-*
453 *graph*, Nucl. Tracks Radiat. Meas **21** (1993), pp. 47.
- 454 [5] M.I.Lopes *et al.*, *Performance analysis based on a Monte-Carlo simulation of a liquid*
455 *xenon PET detector*, IEEE Trans. Nucl. Sci. NS-42, No**6** (1995),pp. 2298-2302.
- 456 [6] E. Aprile *et al.*, *Observation of Anti-correlation between Scintillation and Ionization*
457 *for MeV Gamma-rays in Liquid xenon*, Phys. Rev. B **76** (2007), 014115.
- 458 [7] E. Aprile *et al.*, *Compton Imaging of MeV Gamma-Rays with the Liquid xenon*
459 *Gamma-Ray Imaging Telescope (LXeGRIT)*, submitted to Nucl. Instr. and Meth.
460 A , Vol. **593** (2008), p. 414-425.
- 461 [8] V.Solovov *et al.*, *Two dimensional readout in a liquid xenon ionisation chamber*, Nucl.
462 Instr. and Meth. A **477** (2002), pp.184-190.
- 463 [9] V.M. Atrazhev *et al.*, *Electron Transport Coefficients in Liquid xenon*, IEEE Inter-
464 national Conference on Dielectric Liquids 2005, pp. 329-332.
- 465 [10] K.L. Giboni *et al.*, *Fast Timing Measurements of Gamma-ray Events in Liquid*
466 *xenon*, IEEE Transactions on Nuclear Science, Vol. **52** (2005), No.5, pp. 1800-1804.
- 467 [11] V.N. Solovov *et al.*, *Study of Large Area Avalanche Photodiode for Detecting Liquid*
468 *xenon Scintillation*, IEEE Transactions on Nuclear Science, Vol. **47** (2000), No.4,
469 pp.1307-1310.
- 470 [12] D. Bryman *et al.*, *Reconstruction capabilities of a microPET detector based on Liquid*
471 *Xenon technology*, in preparation.
- 472 [13] O. Bunemann, T.E. Cranshaw, J.A. Harvey, *Design of Grid Ionization Chambers*,
473 Canadian Journal of Research, Vol. **27** (1949), Sec. A.
- 474 [14] Gas Purifiers and Particle Filters, NuPure Corporation, Ottawa ON K2S 1E7
475 Canada
- 476 [15] J.P. Martin, P.A. Amaudruz, *A 48 Channel Pulse Shape Digitizer with DSP*, IEEE
477 Transactions on Nuclear Science, Vol. **53** (2006), No.3.
- 478 [16] Large Area Avalanche Photodiodes (LAAPDs), Advanced Photonics Inc., Camar-
479 illo, CA.
- 480 [17] T. Doke *et al.*, *Absolute Scintillation Yields in Liquid Argon and Xenon for Various*
481 *Particles*, Jpn. J. Appl. Phys., Vol **41** (2002), pp. 1538-1545.

- 482 [18] E. Conti for the EXO Collaboration, *Correlated Fluctuations between Luminescence*
483 *and Ionization in Liquid xenon*, Phys. Rev. B **68** (2003), 054201.
- 484 [19] L.S. Miller, S. Howe, W.E. Spear, *Charge Transport in Solid and Liquid Ar, Kr,*
485 *and Xe*, Phys. Rev., Vol. **166** No. 3, (1968), 871
- 486 [20] H.J. Crawford *et al.*, *Ionization And Scintillation Signals Produced By Relativistic*
487 *La Ions In Liquid Argon*, Nucl. Instrum. Meth. A **256** (1987), 47.
- 488 [21] K. Ni *et al.*, *Performance of a Large Area Avalanche Photodiode in a Liquid xenon*
489 *Ionization and Scintillation Chamber*, Nucl. Instr. and Meth. A, **551** (2005) 356.
- 490 [22] J.L. Rodgers, W.A. Nicewander, *Thirteen Ways to Look at the Correlation Coeffi-*
491 *cient*, The American Statistician, Vol. **42** (1988), pp. 59-66.
- 492 [23] E. Shibamura *et al.*, *Test of the Recombination Model for the Energy Resolution in*
493 *an Ionization Chamber Filled with Liquid Argon or Xenon*, Jpn. J. Appl. Phys., Vol
494 **34** (1995), pp. 1897-1900.
- 495 [24] S. Agostinelli *et al.* [GEANT4 Collaboration], *GEANT4: A simulation toolkit*, Nucl.
496 Instrum. Meth. A **506** (2003), 250.